CRYSTAL GROWTH & DESIGN

pubs.acs.org/crystal

Article

High-Pressure Structural Study on the Effects of Pressure-Transmitting Media on $Bi_{14}MoO_{24}$ and $Bi_{14}CrO_{24}$ Compounds

Pablo Botella,* Josu Sánchez-Martín, Oscar Gomis, Robert Oliva, Samuel Gallego Parra, Julio Pellicer-Porres, Gastón Garbarino, Frederico G. Alabarse, Srungarpu Nagabhusan Achary, and Daniel Errandonea

Cite This: *Cryst. Growth Des.* 2024, 24, 9482−9491

Read Online

ACCESS | Metrics & More | Article Recommendations | Supporting Information

ABSTRACT: An investigation of isostructural compounds $Bi_{14}MO_{24}$, where M is either Cr or Mo, has been conducted under high-pressure (HP) conditions, reaching up to 30 and 40 GPa, respectively. In situ synchrotron X-ray diffraction was employed to monitor alterations in the crystal structure induced by pressure. The compounds have been studied in two different experimental conditions, under hydrostatic conditions using He as pressure transmitting medium (PTM) or under plastic deformation without PTM. Remarkably, the use of helium gas as a PTM revealed isomorphic phase transitions unobserved previously when other PTMs were used. In the case of $Bi_{14}MoO_{24}$, in addition to the previously documented tetragonal ($I4/m$) to monoclinic ($C2/m$) transition, two new isomorphic (monoclinic−monoclinic) phase transitions have been identified. Conversely, $Bi_{14}CrO_{24}$ exhibits two novel isomorphic (tetragonal−tetragonal) transitions preceding the tetragonal-monoclinic transformation. While analogous phase transitions were identified in experiments performed without PTM, an earlier pressure onset of phase transition was noted. Moreover, a new cubic phase coexisting with HP modification was observed in $Bi_{14}CrO_{24}$, providing insights into the behavior of these compounds under extreme conditions of shear-stress.

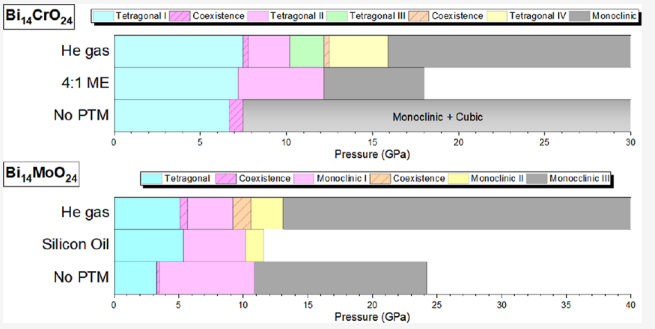

1. INTRODUCTION

In 1753, Johan G. Wallerius discovered the mineral bismite (α-Bi_2O_3) while exploring the Schneeberg mine, though Frondel later suggested it was likely bismuth carbonate. The first confirmed identification of α-Bi_2O_3 came in 1848 by Suckow, leading to extensive research into its polymorphs.[1] Among these, the cubic defect fluorite structure (δ-Bi_2O_3) is notable for its high oxygen ion conductivity, although it is only stable at high temperatures. However, the δ-phase can be stabilized at room temperature by dopants.[2−4]

The study of Bi-M-O systems, where M is a pentavalent or hexavalent transition metal, has led to the synthesis of defect fluorite superstructures in the δ-Bi_2O_3 phase.[5,6] Compounds like $Bi_{14}MO_{24}$ (M = Cr, Mo, W) are particularly promising for photochemical catalysts due to their high ionic conductivity, influenced by the presence of lone-pair electrons (LPEs).[7−9] Pressure can further modify the structure and impact of LPEs, as seen in Bi_2O_2S, where applying pressure led to a phase transition from 2D to 3D topology.[10,11]

High-pressure studies reveal significant effects of pressure-transmitting media (PTM) on the structural evolution of these materials. Without PTM, samples may undergo plastic deformation under shear stress, leading to novel transformations.[12] In addition, in situ high-pressure X-ray diffraction (HP-XRD) characterization is crucial as some phases may disappear after pressure release.[13] For instance, the transformation of graphite to hexagonal diamond along with the coexistence of cubic diamond as a distinct phase, was shown to be partially reverted upon decompression.[14,15]

This research extends the investigation of $Bi_{14}CrO_{24}$ and $Bi_{14}MoO_{24}$ to pressures up to 40 GPa, exploring structural changes under two extreme conditions, high hydrostaticity with helium as PTM to high plasticity without PTM. Helium not only helps to generate hydrostatic conditions but could permeate the crystal structure of the studied compounds affecting the compressibility and deformation of the crystal structure.[16,17] Conversely, plastic deformations could induce structural changes different from hydrostatic compression.[18] The results are discussed in the context of previous findings,[19,20] providing insights into the behavior and stability of these compounds under extreme conditions.

Received: July 3, 2024
Revised: November 5, 2024
Accepted: November 5, 2024
Published: November 12, 2024

https://doi.org/10.1021/acs.cgd.4c00904
Cryst. Growth Des. 2024, 24, 9482−9491

Table 1. Lattice Parameters of the Synthesized Samples of $Bi_{14}MO_{24}$ Preloaded into the DAC[a]

sample	$Bi_{14}CrO_{24}$		$Bi_{14}MoO_{24}$	
experiment	No PTM (0.49 GPa)	He gas (0.5 GPa)	No PTM (0.7 GPa)	He gas (0.4 GPa)
a (Å)	8.630(2)	8.645(3)	8.592(5)	8.674(4)
c (Å)	17.156(4)	17.169(6)	17.104(6)	17.268(5)
volume (Å^3)	1278.23(5)	1284.30(9)	1258.97(2)	1299.23(2)

[a]Pressures and PTM are indicated.

2. EXPERIMENTAL PROCEDURE

2.1. Sample Synthesis. Powder samples of $Bi_{14}MO_{24}$ have been synthesized through a solid−state reaction method involving the precursors of Bi_2O_3 (Alfa Aesar, 99%), MoO_3 (Alfa Aesar, 99%), and Cr_2O_3 (99% Sigma-Aldrich) in stoichiometric proportions. Before mixing, the reagents underwent drying and were thoroughly blended using an agate mortar. Subsequently, the mixture was pestled and pressed into pellets. These pellets were then loaded into a platinum boat and subjected to heating at 973 K for 12 h. The heating and cooling process for high-temperature reactions followed a rate of 2 °C per minute (see refs 19, 20, for more details on the synthesis).

2.2. High-Pressure XRD Measurements. For a nonhydrostatic experiment, $Bi_{14}CrO_{24}$ was loaded into an Almax diamond anvil cell (DAC) with a culet size of 500 μm. The pressure chamber was drilled using an electrical discharge machine in a stainless-steel gasket, measuring approximately 200 μm in diameter and 55 μm in height. For the $Bi_{14}MoO_{24}$ sample, a DAC with a 350 μm culet size was selected. A rhenium gasket for the sample chamber, measuring 150 μm in diameter and 35 μm in height, was used. Additionally, to monitor pressure, a ruby sphere along with Cu was inserted alongside the sample powder.[21,22] No PTM was included in these experiments. Angle-dispersive XRD measurements under pressure were carried out at room temperature at the XPRESS beamline of the Elettra storage ring.[23] A monochromatic X-ray beam of 0.4956 Å and a spot size of 80 μm in diameter has been used for the measurements. The diffracted patterns were acquired with a PILATUS 3S 6 M detector (from DECTRIS) having a sample−detector distance of 939.50 mm and using LaB_6 as standard.

The hydrostatic experiments were performed at the European Synchrotron Radiation Facility (ESRF), using ID15B beamline for powder XRD measurements. The sample was 300 mm away from the detector Eiger2 × CdTe 9 M (DECTRIS). The X-ray wavelength was 0.41 Å and the beam size of 1 × 1 μm.[24] For both samples a membrane-type DAC was used. For the loading, 200 μm rhenium gaskets were indented to a thickness of 60 μm and a chamber of 125 μm diameter was drilled in the center. The culet size of the diamonds was 350 μm. A Cu sphere was included in the chamber to measure the sample pressure. Helium was used as PTM.

The data collected at both synchrotron facilities have been integrated into conventional diffractograms using the Dioptas software.[25] The Rietveld refinements and Le Bail fits of the integrated XRD patterns have been performed using the GSAS-II software.[26] The Vesta software has been used for structural representation.[27]

3. RESULTS AND DISCUSSION

3.1. Raw Material Structure. The as-synthesized samples of $Bi_{14}MO_{24}$, which have been preloaded into the DAC for the two sets of experiments, at a pressure close to 0.5 GPa, exhibit a tetragonal structure ($I4/m$), in agreement with those reported in the International Crystal Structure Database (ICSD) entries 97483 ($Bi_{14}CrO_{24}$) and 280114 ($Bi_{14}MoO_{24}$) (see Tables S1 and S2 in the Supporting Information for more details). The corresponding Rietveld refinement can be seen in the Supporting Information (Figures S1 and S2). The goodness-of-fit (χ^2) and R factors (R_{wp} and R_p) are also presented in Table S3 in the Supporting Information.[28] The obtained lattice parameters are presented in Table 1. The lattice parameters align closely with those documented in the literature.[9,19,20,29] The body-centered tetragonal superstructure having a subcell of the δ-Bi_2O_3 phase fluorite is intricately formed through the assembly of various polyhedra units comprising Bi−O and M-O bonds. Within this structure, M-O bonds exhibit significant orientation disorder, with tetrahedral coordination occurring at both the corners and center of the unit cell. The remaining space in the structure is filled by Bi−O units, with two distinct coordination geometries due to the LPEs role: BiO_4 (Bi1 (8h) and Bi3 (4e)) square pyramids and Bi2 (16i) trigonal bipyramids, also could be seen as distorted tetrahedral. The individual square pyramids of Bi1 and Bi3 atoms share their O−O edges forming Bi_6O_8 clusters (see Figure 1, and Supporting Information Tables S1 and S2). The

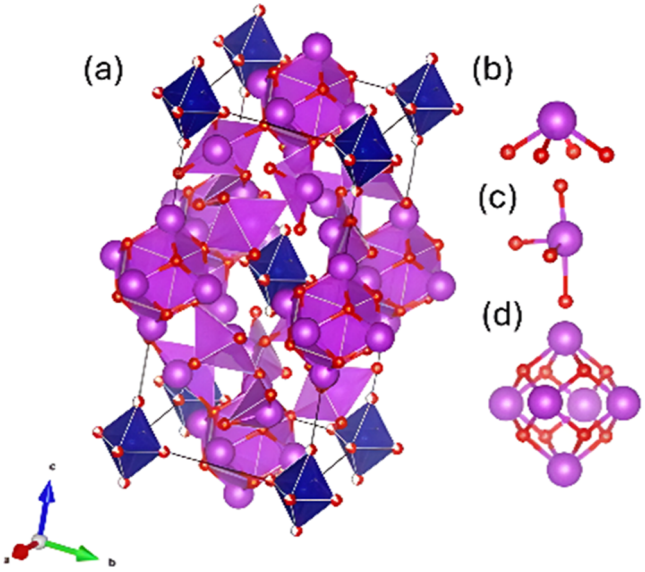

Figure 1. (a) Crystal structure of the body-centered tetragonal with space group ($I4/m$) of $Bi_{14}MO_{24}$. (b) BiO_4 square pyramids. (c) Trigonal bipyramid. (d) Bi_6O_8 cluster. Partially colored atoms represent the partial occupancy of oxygen atoms.

M atom within this framework undergoes a slight displacement along the c-axis, occupying the 2a site with a half occupancy. This site configuration can also be interpreted as an octahedral coordination, wherein one axial and one equatorial oxygen site remain vacant, resulting in a four-coordinated polyhedron, $MO_4\square_2$. Notably, the lattice's loosely packed nature provides room for the rotationally disordered tetrahedra to integrate into the structure.[5,19,20,29]

3.2. High-Pressure Study of $Bi_{14}MoO_{24}$. Under compression, the tetragonal structure undergoes volume contraction attributed to the pronounced compressibility of the larger Bi−O bond in the trigonal pyramid polyhedron, coupled with a reduction in the distances between the Bi and O atoms along the direction of LEP of Bi.[20] Specifically, in the

https://doi.org/10.1021/acs.cgd.4c00904
Cryst. Growth Des. 2024, 24, 9482−9491

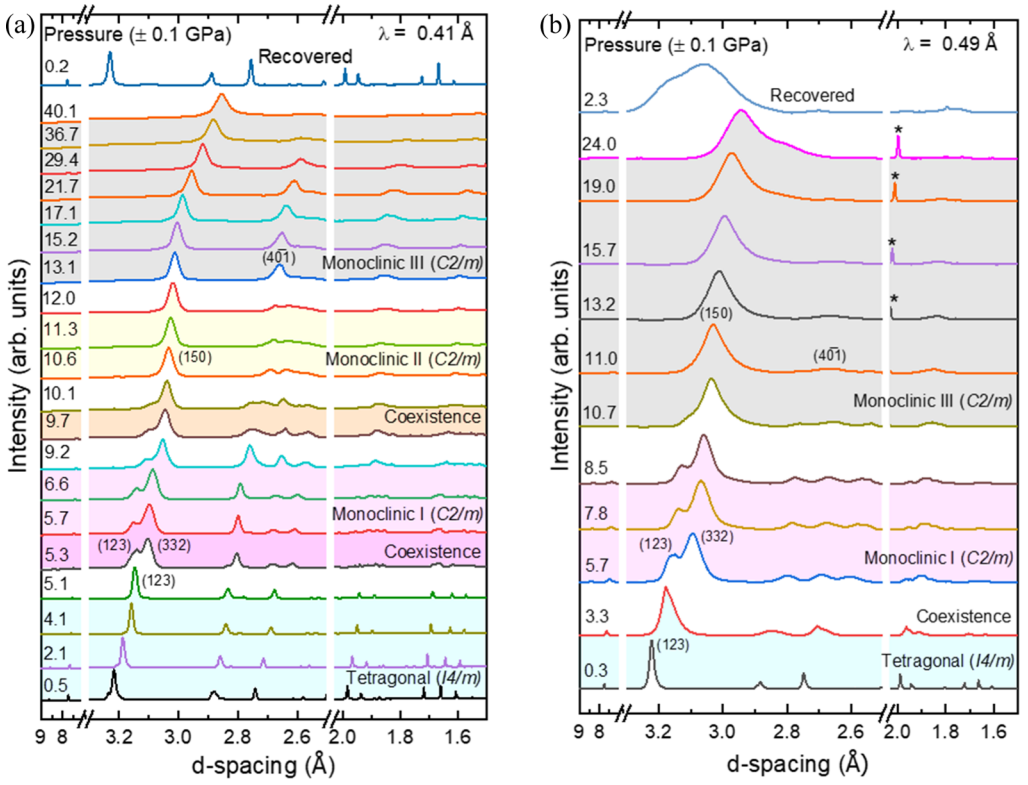

Figure 2. (a) Selected XRD patterns of $Bi_{14}MoO_{24}$ up to 40.1 GPa using He as PTM. (b) Experiment using no PTM up to 24 GPa. Different shading colors are used to distinguish the different structures and phase coexistence indicated on the plot. (*) Stands for the rhenium gasket signal. Notice that the *x*-axis is reverted.

case of $Bi_{14}MoO_{24}$ utilizing He gas as a PTM, the tetragonal structure remains stable up to 5.1 GPa (see Figure 2a and Table S4 in the Supporting Information). Beyond this pressure, discernible changes occur in the XRD pattern, notably evidenced by the splitting of the (123) reflection into two distinct reflections (123) and (332), which is accompanied by the emergence of additional reflections at higher angles (lower *d*-spacing). These alterations are similarly observable in experiments conducted without a PTM (see Figure 2b). However, an earlier onset of the pressure-induced changes is observed due to the contribution as a shoulder on the reflections, especially on reflection (123), indicating already a phase coexistence at 3.3 GPa. Although, the tetragonal phase is still the predominant one (see Figure S3 in Supporting Information). Analogous variations in the XRD pattern are noted during the phase transition of the same compound when employing silicon oil at 5.4 GPa.[20] The high-pressure phase is characterized as monoclinic I ($C2/m$), mirroring the structure observed at low temperatures in $Bi_{14}MoO_{24}$ (ICSD 97485) by Crumpton et al.[29] The identification of the high-pressure phase with the low-temperature phase is consistent with the widespread phenomenon of opposite influence of isothermal compression and isobaric expansion on phase transitions which has been documented in various materials.[30,31] The monoclinic phase was fitted by the Le Bail procedure and the results are shown in the Supporting Information (Figures S4 and S5). Lattice parameters and volume will be discussed further in the text.

On further compression, a second phase transition takes place around 9.7−10.1 GPa in experiments where He gas was used as PTM. The main change in the XRD pattern is that the reflections (123) and (332), start to merge into one broad reflection (150). Also, the reflections at higher angles (lower *d*-spacing) start to merge and broaden. This phase transition is identified also as monoclinic II, sharing the same space group as the monoclinic I phase. This observation serves to definitively corroborate our prior findings. Previously, we elucidated a phase transition occurring around 11.5 GPa utilizing silicon oil as PTM, with only one high-pressure data point available at the time. Twenty Therefore, it is reasonable to infer that this transition is not triggered by the hydrostatic limit of the PTM, given that helium remains quasi-hydrostatic at the transition pressure.[32] At a pressure of 13.1 GPa, a second isomorphic transition (to monoclinic III phase) was observed, as indicated by the appearance of the reflection $(40\bar{1})$ in Figure 2a. There was not only an increase in the intensity of this reflection as the pressure increased, but also the *d*-spacing variation rate of the reflection (150) dropped from 0.0102 to 0.0059 Å/GPa across the phase transition. It can be noted that this phase remains stable up to the maximum pressure of 40.1 GPa.

Similar behavior was noted within the pressure range of 8.5−10.7 GPa in the experiment performed without PTM (see Figure 2b). An isomorphic transition was observed, but in this case, the transition is directly from the monoclinic I phase to the monoclinic III phase observed under hydrostatic conditions at 13.1 GPa. Knowing the offset of 2 GPa for the transition from tetragonal to monoclinic I under non-hydrostatic conditions, it is plausible to infer that under nonhydrostatic conditions, the structural transition proceeds directly from monoclinic I to monoclinic III. This is possible as the pressure range of the existence of monoclinic II is about 3 GPa, as it could be observed in the experiment with He as PTM. Furthermore, upon further compression, no additional

https://doi.org/10.1021/acs.cgd.4c00904
Cryst. Growth Des. 2024, 24, 9482−9491

phase transition is discernible in the pressure range explored up to the maximum pressure of 24 GPa. This phenomenon could be attributed to nonhydrostatic conditions. Without PTM deviations of hydrostatic conditions of a few GPa are to be expected, either in the form of pressure gradients or as nondiagonal components of the stress tensors.

At the top of the Figure 2a,b, the recovered XRD pattern is shown for both experiments. For He gas as PTM, the starting crystal structure is recovered demonstrating a reversible process. On the other hand, the recovered pattern from the experiment with no PTM presents a pattern like that of the monoclinic I phase. It has been identified the recovered phase as monoclinic I due to the presence of two reflections (123) and (332) (see Figure S6 in Supporting Information), which are characteristic of this phase. It shows broader peaks attributed to the high shear-stress suffered. Furthermore, Figure 3 depicts the sample chamber before and after the pressure cycle, highlighting the transformation in the sample's appearance from white to dark gray powder.

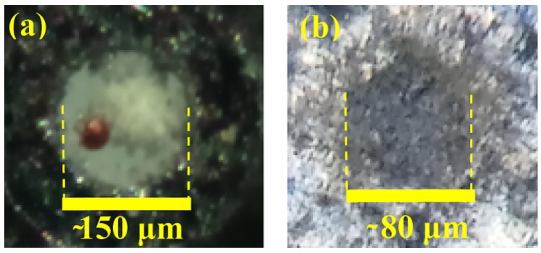

Figure 3. (a) Starting white powder of $Bi_{14}MoO_{24}$ sample together with a Cu chip as pressure calibrant in the sample chamber. (b) Recovered a dark gray powder sample after the HP experiment without PTM. The hole shrank during the experiment. Pictures taken from a Phonés camera under the microscope.

3.2.1. Lattice Parameters and Volume Evolution under Pressure of $Bi_{14}MoO_{24}$. The evolution of lattice parameters and the β-angle under pressure are represented in Figure 4a,b. These data were obtained through XRD pattern refinement techniques. Specifically, the Rietveld method was utilized solely for refining the tetragonal phase, while the Le Bail method was employed for analyzing the other phases (see Supporting Information). Due to the substantial presence of oxygen vacancies leading to partial occupancy and the number of atoms present, refinement of atomic positions was unattainable. Consequently, the positions were adopted from Crumpton et al.[29] ($Bi_{14}CrO_{24}$) and Ling et al.[9] ($Bi_{14}MoO_{24}$) work. As the XRD reflections broaden under pressure, especially in the case without PTM, the error bar was estimated by refining multiple iterations of the XRD pattern analysis, ensuring a higher degree of reliability compared to the error provided solely by the software (in this case, GSAS-II was employed).[26]

In the tetragonal phase, the lattice parameters *a*-axis and *c*-axis demonstrate a consistent linear relationship (coefficient of determination $R^2 = 0.99$). Experimental data with He gas as PTM indicate axial compressibilities of $\kappa_a = 5.5(2) \times 10^{-3}$ GPa^{-1} and $\kappa_c = 3.1(2) \times 10^{-3}$ GPa^{-1}. However, when employing silicon oil,[20] the compressibility values shift slightly to $\kappa_a = 4.8(1) \times 10^{-3}$ GPa^{-1} and $\kappa_c = 3.7(2) \times 10^{-3}$ GPa^{-1}. These variations, which could be due to the possibility of the He penetration in the structure, will directly impact the equations of state (EoS), influencing the bulk modulus as discussed further in the text.[16] Such phenomenon will not be surprising in compounds with vacancies in the crystal structure as those here studied.[17] Notice that only two data points are available for the tetragonal phase without PTM, as depicted in Figures 2b and 4a. Thus, no reliable analysis can be done in this case. To clarify this issue further studies using a selection of penetrating and nonpenetrating PTM and following small pressure steps are needed. This is beyond the scope of the present study. After undergoing the structural phase transition, the axis originating from the tetragonal phase can undergo modifications, as illustrated in Figure 5. Consequently, the *c*-axis transforms directly into the *b*-axis of the monoclinic phase. Conversely, the *a*-axis of the tetragonal phase bifurcates into the *c*-axis and $a/\sqrt{2}$-axis within the monoclinic phase. In the monoclinic I phase, the *b*-axis is the most affected by the choice of PTM while the others follow a similar trend. Despite the presence of data points exhibiting higher dispersion, a general linear trend remains applicable for describing the

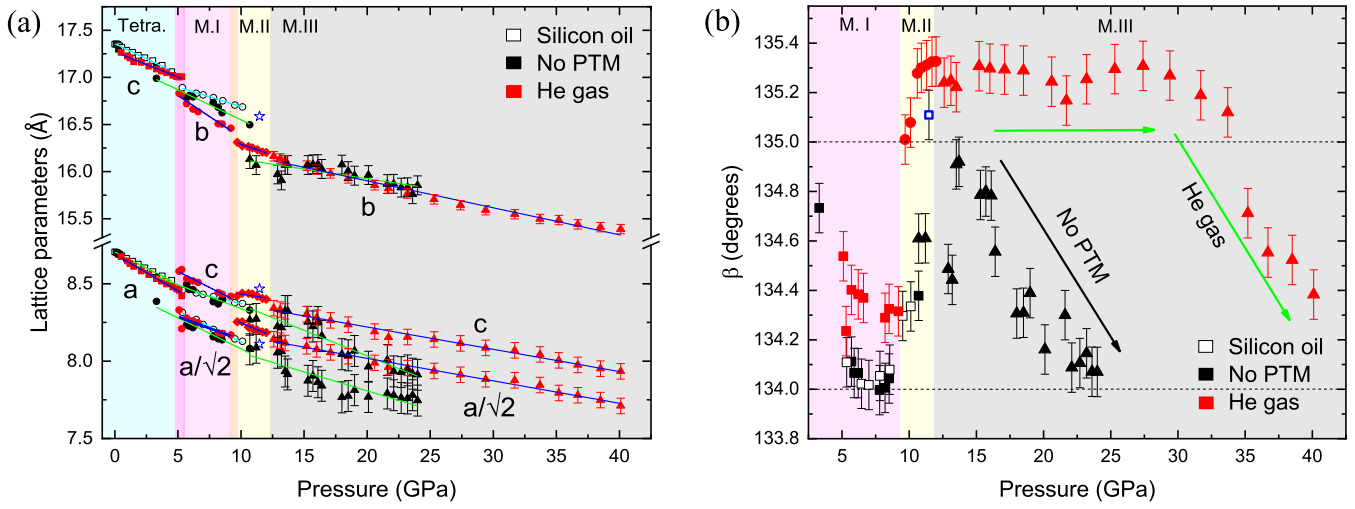

Figure 4. (a) Lattice parameters as a function of pressure for $Bi_{14}MoO_{24}$ obtained through experiments employing various PTMs. Linear fits for visual guidance. (b) β-angle vs pressure measurements across various monoclinic phases employing diverse PTMs. The color code is the same as Figure 2 (M stands for monoclinic). Data for the Silicon oil experiment was taken from ref 20.

https://doi.org/10.1021/acs.cgd.4c00904
Cryst. Growth Des. 2024, 24, 9482−9491

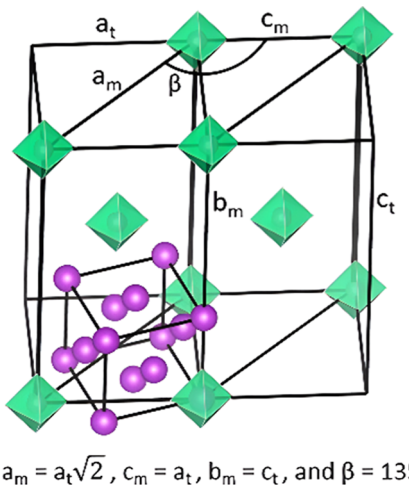

Figure 5. Transformation from the body-centered tetragonal to the C-centered monoclinic structure (polyhedra units of $MoO_4\square_2$ are shown in green) and the unit-cell of δ-B_2O_3, which is related to the tetragonal supercell. In the unit-cell parameters, t and m stand for tetragonal and monoclinic, respectively. Image from ref 20.

evolution under pressure. Notably, the steepest slope is seen in the experiment with He gas as PTM, followed by no PTM and silicon oil experiments, respectively. At the monoclinic I to monoclinic II phase transition, the lattice parameter experiences a discontinuity as can be seen in He gas as PTM experiments. The *b*-axis parameter jumps to lower values and the *c*-axis and *a*-axis to higher values. Interestingly, a similar behavior was observed in our previous work using silicon oil (star dots in Figure 4a).[20] The final phase transition also exhibited a discontinuity in the lattice parameters, albeit not as abruptly as observed in the preceding transition. It can be observed that in experiments without PTM, where the phase transition occurs directly from monoclinic I to monoclinic III, the lattice parameter *b*-axis exhibits a behavior similar to that seen in experiments involving He gas as PTM. However, in this scenario, the parameters *c*-axis and *a*-axis are more significantly affected, displaying a more pronounced linear trend. This could be due to the shear planes along the *a*-axis and *c*-axis of the monoclinic phase, which are more affected by the nonhydrostatic conditions.

The β-angle of the monoclinic phase mirrors these structural alterations. In Figure 4b, it is evident that the monoclinic I phase exhibits the least sensitivity to the choice of the PTM, showing similar behavior across different conditions. However, it is worth noting that experiments involving He gas as PTM demonstrate higher values. As mentioned earlier, within this phase, the unique *b*-axis appears to be the most influenced by the choice of the PTM, as illustrated in Figure 4a. Thus, it is reasonable that in this phase the angle is less affected by the choice of PTM. A sudden increase in the β-angle is observed at the phase transition from the monoclinic I phase to the monoclinic II phase, corresponding to the abrupt discontinuity in the lattice parameters. After this transition, the β-angle follows different paths for the different PTMs and without PTM. In the case of He gas as PTM, the β-angle remains stable at around 135.3° showing a linear behavior until[34] GPa where a sudden drop is observed. On the contrary, in the experiments without PTM where shear-stresses have a huge influence on the structure, the β-angle already drops following a similar trend as in the He gas as PTM experiment but with an earlier pressure onset. It is worth noticing that our previous estimation of the angle using silicon oil also experienced this jump in value (blue empty square in Figure 4b).[20]

The unit-cell volume versus pressure, along with the corresponding EoS fit, is depicted in Figure 6a. A notable disparity emerges in the evolution of unit-cell volume under pressure between He and silicon oil as PTMs. As mentioned previously, this discrepancy could be due to the diffusion of He atoms into the crystal structure. It is worth noting that the two data points obtained without a PTM in the experiment align with the data set of the silicon oil experiment. Following the phase transition from tetragonal to monoclinic I, there is a volume collapse (not considered phase coexistence in the analysis) of approximately 2.3% when He is used as the PTM.

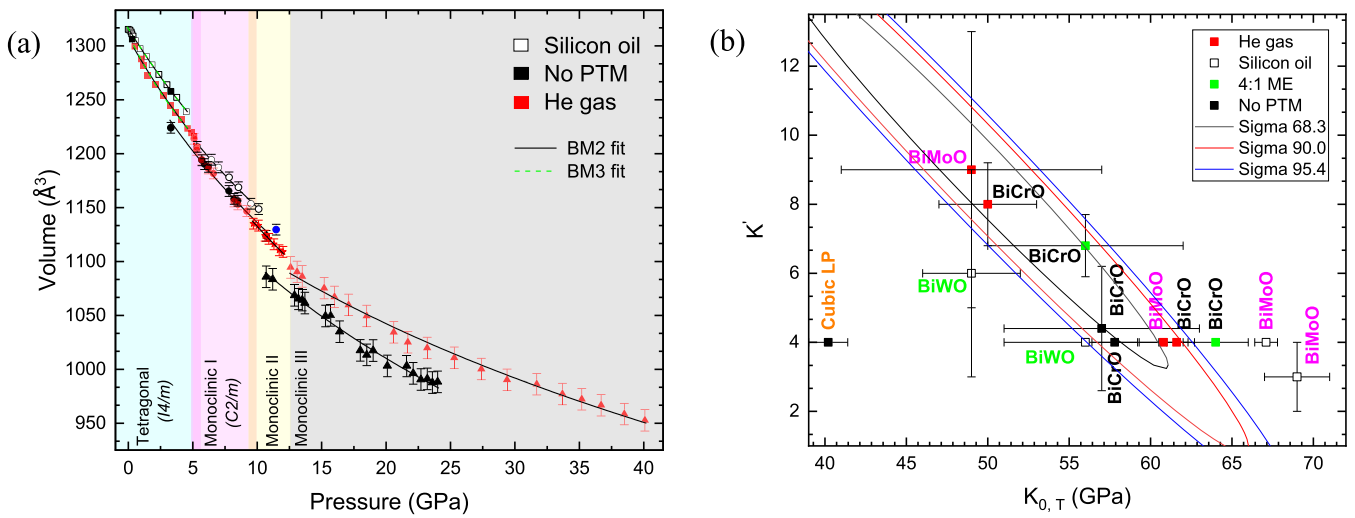

Figure 6. (a) Unit-cell volume evolution under pressure for $Bi_{14}MoO_{24}$. Black solid line shows second order BM EoS fit. Green dashed line shows third order BM EoS fit. (b) The bulk modulus of the tetragonal phase for isomorphic compounds using different PTMs and without PTM as indicated is shown. Confidence ellipses for the bulk modulus estimated using He as PTM for the $Bi_{14}MoO_{24}$ compound are included. The color code is the same as Figure 4. Data for 4:1 methanol−ethanol (ME) and silicon oil as PTM experiments are taken from refs 19 and 20, respectively. Unpublished data for $Bi_{14}MoO_{24}$ compound.

https://doi.org/10.1021/acs.cgd.4c00904
Cryst. Growth Des. 2024, 24, 9482−9491

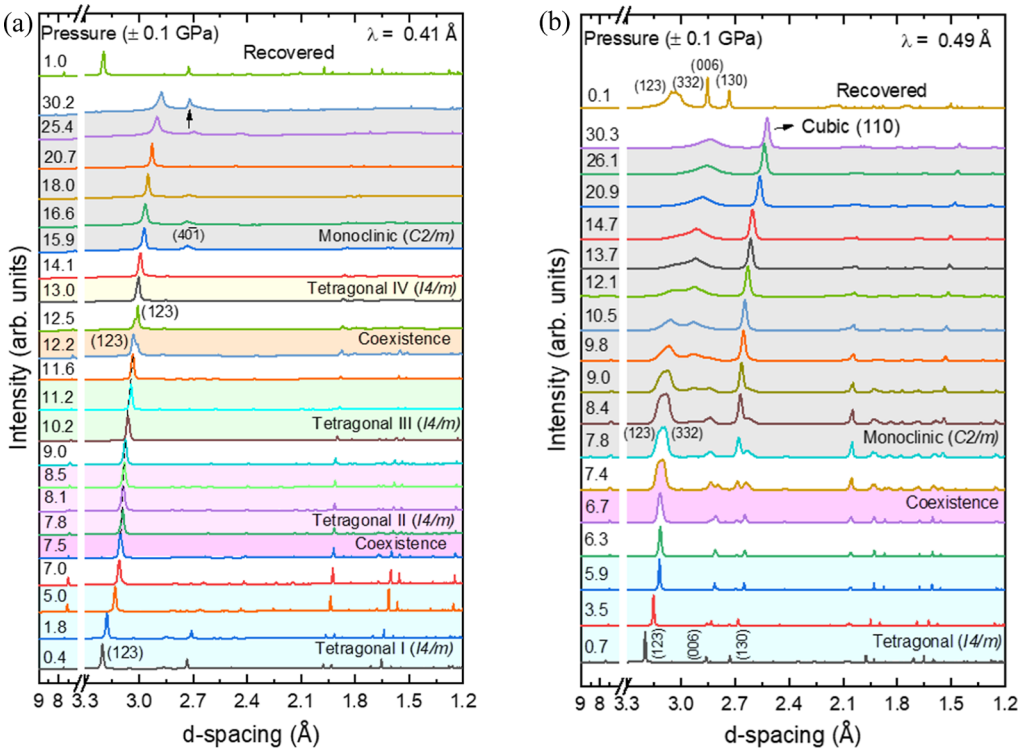

Figure 7. (a) Selected XRD patterns of $Bi_{14}CrO_{24}$ up to 30.2 GPa using He as PTM. (b) Experiment using no PTM up to 30.3 GPa. Different shading colors are used to distinguish the different structures and phase coexistence indicated on the plot. Cubic indicates the reflection belongs to this phase. Notice that the *x*-axis is reverted.

Note that the volume undergoes smooth changes during the phase coexistence from one phase to another, demonstrating a second-order phase transition, contrary to what was observed using other PTMs such as silicon oil or no PTM, although, additional data points throughout the transition are needed to conclusively validate this assumption. Consequently, this volume collapse appears to be less abrupt compared to that of 2.7% observed when silicon oil or no PTM is employed. Interestingly, after the phase transition, the data from experiments without PTM and He as PTM follows a similar EoS. A slight volume collapse of 1% is observed at the monoclinic I to monoclinic II transition when He is used as PTM. In the case of silicon oil as PTM, this collapse was about 1.6%. As mentioned previously, the experiment with no PTM, went directly from monoclinic I to monoclinic III experiencing a volume collapse of 3.4%. From this volume collapse, the sample experienced a different volume evolution under pressure compared to the experiment under He as PTM. In the last transition in He as PTM experiments, the collapse was 1.4%. It can be noticed that the sample undergoes smooth transitions using He as PTM compared to silicon oil as PTM or no PTM due to the role of nonhydrostaticity conditions. Now, it is evident that in our previous work,[20] it was provided evidence of the phase transition from monoclinic I to probably monoclinic II, a phase clearly observed in the experiments using He as PTM. The bulk modulus of the tetragonal phase for isostructural compounds ($Bi_{14}MoO_{24}$, $Bi_{14}CrO_{24}$, $Bi_{14}WO_{24}$) is plotted in Figure 6b. To compare with the already existing bulk modulus data in the literature, Birch–Murnaghan EoS of second-order (BM2) and third-order (BM3) have been used. The confidence ellipses, up to 3σ, have been constructed for the bulk modulus of the $Bi_{14}MoO_{24}$ compound using He as PTM. More data are within the 3σ confidence ellipse. No significant differences are observed among compounds with different transition metal cations or PTMs used. It is evident that all the data, whether estimated by BM2 or BM3 EoS, fall within a bulk modulus range of 40 to 70 GPa. This is consistent with our previous assumption that the bulk modulus of these compounds is dominated by the polyhedra of bismuth and not due to the highly incompressible tetrahedral units formed by the transition metals.[19,20] The variations in bulk modulus primarily stem from the presence of stereochemically active $6(s/p)^2$ LPEs within the different structural configurations of bismuth (see Figure 1). Additionally, the influence of the PTM plays a significant role in modulating this behavior. The bulk modulus for the monoclinic phases, together with the tetragonal phase, is shown in Table S6. In this case, the BM2 EoS has been used as not so many points are available for phases I and II, and for consistency with literature.[19,20] However, for phase III, a higher-order BM equation could be more suitable. As discussed previously, He as PTM and no PTM experiments present similar values for the bulk modulus of monoclinic I and II phases. A considerable difference can be noticed for phase III, especially for He as PTM experiments where the bulk modulus increased up to 109(4) GPa.

3.3. High-Pressure Study of $Bi_{14}CrO_{24}$. For the case of $Bi_{14}CrO_{24}$, the tetragonal phase exhibits remarkable stability, persisting up to 14 GPa, as evidenced by Figure 7a (see also Table S5 in the Supporting Information). In contrast to the observations in $Bi_{14}MoO_{24}$ when He is used as PTM. Several isomorphic transitions, up to four, all belonging to the same space group ($I4/m$), are observed preceding the phase transition from the tetragonal to the monoclinic phase. One potential explanation for these observations might be that under ambient conditions, the most stable phase of the

https://doi.org/10.1021/acs.cgd.4c00904
Cryst. Growth Des. 2024, 24, 9482−9491

compound $Bi_{14}CrO_{24}$ is tetragonal (monoclinic phase at T ~275−200 K). However, for the compound $Bi_{14}MoO_{24}$ under ambient conditions, the energy levels of the tetragonal and monoclinic (T ~295 K) phases are very close, as demonstrated by experiments conducted by Crumpton et al.[29] Thus, when pressure is applied, the $Bi_{14}MoO_{24}$ compound is more prone to transform into a monoclinic structure compared to $Bi_{14}CrO_{24}$ compound. The transformation from tetragonal I to tetragonal II is evidenced by a phase coexistence, where the (123) reflection broadens (pattern at 7.5 GPa) and only a residual shoulder can be appreciated in the pattern at 7.8 GPa. This phase transition was previously observed by Errandonea et al. at similar pressures.[19] The changes in the isomorphic transformations are subtle and it can be noticed by the change in the reflection position under pressure (dashed lines in Figure 7a), especially in the case of the transformation from phase II to III, where a change in the slope can be noticed from 0.014 to 0.018 Å/GPa. Only the transformation from tetragonal III to tetragonal IV is clearly shown by the phase coexistence (patterns at 12.2 and 14.1 GPa). The (123) reflection splits in two, one reflection from phase III and the other from phase IV. Only one of the two reflections is observed after the transformation is completed. At 15.9 GPa, the $(40\bar{1})$ reflection in Figure 7a, indicates a phase transition to a monoclinic structure, similar to what was observed in $Bi_{14}MoO_{24}$ the monoclinic phase belongs to the same space group ($C2/m$). Remarkably, the tetragonal phases III and IV were not previously observed using 4:1 methanol−ethanol (ME) mixture as PTM by Errandonea et al.[19] These differences could be attributing to the penetration of He in the structure giving major structural stability. In addition, the present experiment with no PTM presents a direct transformation to the monoclinic ($C2/m$) phase without going through all the tetragonal isomorphic transformations observed in the experiment where He is used as PTM (see Figure 7b). In this compound, it seems that the higher the hydrostaticity of the PTM is, the higher the transition pressure to the monoclinic phase, considering, in the case of He as PTM, the possibility of penetration into the structure. Contrary to what was observed in the case of the $Bi_{14}MoO_{24}$ compound, where the pressure transition from tetragonal to monoclinic is almost independent, at least for silicon oil and He as PTM, and with a pressure offset of 2 GPa for the experiment without PTM. In the case of $Bi_{14}CrO_{24}$, the pressure offset was about 8 GPa, demonstrating higher strain−stress effects on the sample. That is evidenced by the formation of a new phase never previously reported, which is identified as body-centered cubic belonging to the space group $Im\bar{3}m$ (number 229) (reflection (110) in Figure 7b as Cubic). See Supporting Information (Figure S7) for the indexing of the whole pattern at 13.7 GPa using Cu, new cubic phase, and $Bi_{14}CrO_{24}$ phases. This new phase was obtained after indexation of the new appearing peaks, which leads to a body-centered cubic structure related to the cubic structure of Nd_2O_3 and La_2O_3.[33] In this structure, the 2a Wyckoff position is randomly occupied by Bi and Cr atoms with occupations of 14/16 and 1/16, respectively, and the 6c Wyckoff position is partially occupied by O atoms with a partial occupation of 1/2. Such disordered cubic structures have been also found in other fluorite-related oxides under high-pressure conditions.[34] Furthermore, the heightened intensity of the reflection, indicated by the arrow in Figure 7a of the latest measured pattern, may suggest the onset of a new phase transition, akin to the transition observed from monoclinic II to III in the $Bi_{14}MoO_{24}$ compound.

After pressure was released (Figure 7a,b, top), the pattern from the starting sample was recovered in the case of the He experiment. However, the main reflection appears to be asymmetric compared to the reference pattern at 0.4 GPa. Thus, the crystal structure was recovered but it has suffered some distortion after the high-pressure cycle. For the experiment without PTM, we recovered a mixture of products. The reflections (006) and (130) are indications of partially recovered the initial tetragonal phase, supported by the recovered sample which presents an orange color (see Figure 8b). The reflections (123) and (332) are signs of the monoclinic I phase, also supported by the dark-gray color in Figure 8b. In the recovered pattern, it has not been observed contribution of the cubic phase, showing their metastability under high shear-stress conditions. However, further investigations are needed to explore this new phase under high-pressure and shear-stress conditions.

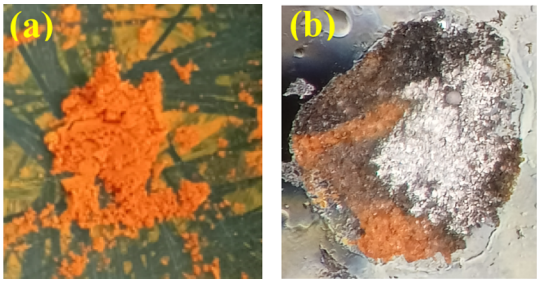

Figure 8. (a) Starting orange powder of $Bi_{14}CrO_{24}$ sample on agate mortar. (b) Recovered orange/black/metallic powder sample after the HP experiment without PTM. Pictures taken from a Phone's camera under the microscope.

3.3.1. Lattice Parameters and Volume Evolution under Pressure of $Bi_{14}CrO_{24}$. Lattice parameters, β-angle, and unit-cell volume evolution under pressure are presented in Figure 9a−c, respectively. The tetragonal phase I follows a similar trend independently of the PTM used. This is reflected in the bulk modulus which has a little variation from 50 to 58 GPa as can be observed in Figure 6b (confidence ellipses plot). After the initial phase transition to the tetragonal II phase, corresponding to the phase previously observed by Errandonea et al.[19] as tetragonal I′, with similar initial volume and bulk modulus (see Table S7 in the Supporting Information), we obtained the lattice parameters of the tetragonal phases which are shown in Figure 9. In the experiment without PTM, the lattice parameters of the cubic phase can be followed up to the maximum pressure reached. Interestingly, from phases III and IV, our data using He as PTM deviates from the data using a 4:1 ME mixture due to the two newly observed isomorphic transitions. This could also be seen as a sign of the possible He penetrations of the crystal structure. A pressure offset difference of about 4 GPa is noticed from the tetragonal to monoclinic transition using ME mixture as PTM. The β-angle presents similar qualitative behavior as observed for $Bi_{14}MoO_{24}$, a sudden increase reaching values around 135.3° followed by a drop. It has been observed that when using ME as PTM, the final data point measured exhibits an increase in value, even though no further data was available. The bulk modulus of all the high-pressure phases has been determined using BM2 EoS for the same reason as commented previously.

https://doi.org/10.1021/acs.cgd.4c00904
Cryst. Growth Des. 2024, 24, 9482−9491

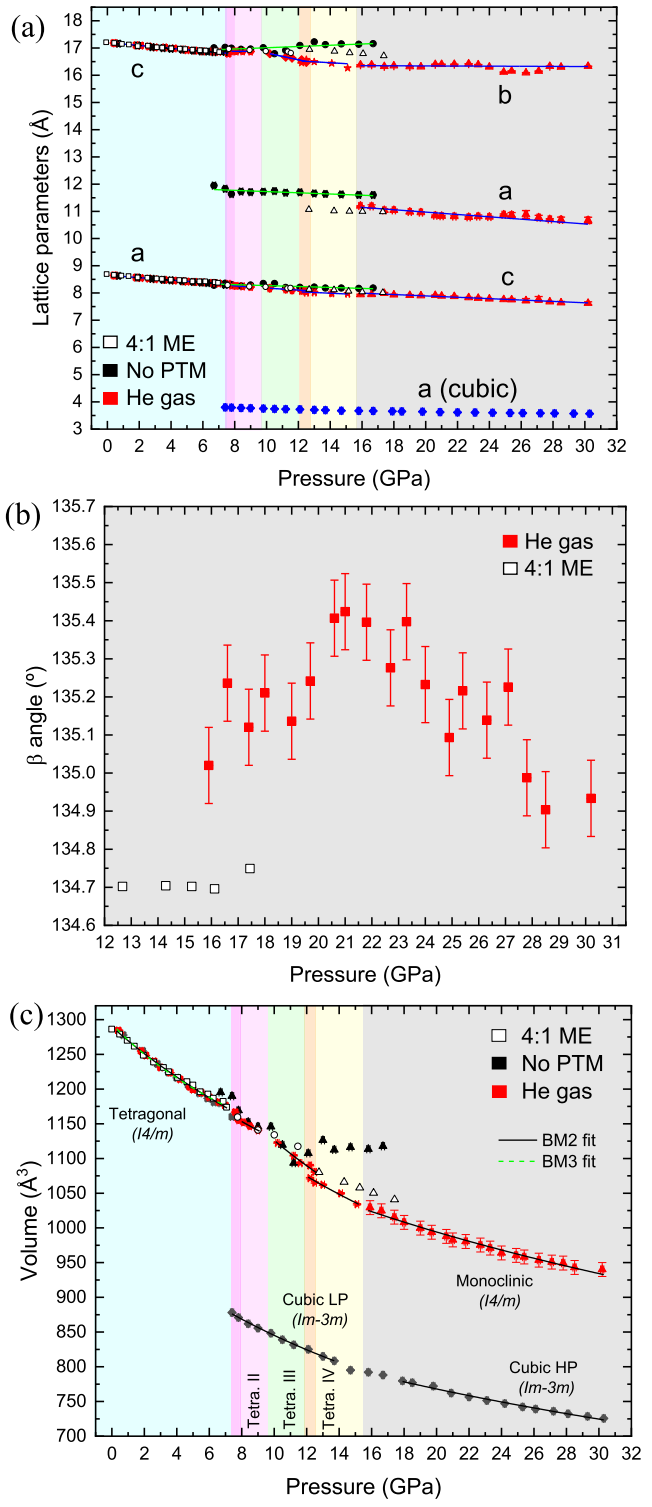

Figure 9. (a) Lattice parameter vs pressure for $Bi_{14}CrO_{24}$ obtained through experiments employing various PTMs. Linear fits are given for visual guidance. (b) β-angle measurements vs pressure for the monoclinic phase employing diverse PTMs. (c) Unit-cell volume evolution under pressure. Black solid line shows second order BM EoS fit. Green dashed line shows third order BM EoS fit. The color code follows the same pattern as Figure 7a. The volume of the cubic phase is multiplied by 16. Data for the 4:1 ME experiment was taken from ref 19.

All the results are shown in Table S7 in the Supporting Information. A similar bulk modulus has been obtained for the monoclinic phase using He or ME as PTMs. Due to the phase coexistence and the huge strain−stress suffered by the sample, we were unable to follow properly the lattice parameters at all pressures in the experiments without PTM. Until it was possible, the lattice parameters were retrieved showing a plateau after 12 GPa (Figure 8a,c). It was observed that the plateau also existed in the cubic phase. As a result, two phases were distinguished: the low-pressure (LP) phase and the higher-pressure (HP) phase. These phases were analyzed using a BM2 equation. However, further investigations are encouraged to explore the formation of this new phase. Dedicated diamond anvil cells for high shear stress, such as rotational DACs, can be used for this purpose.[35]

4. CONCLUSIONS

The impact of pressure-transmitting media on phase transitions in $Bi_{14}MO_{24}$ (M = Cr, Mo) compounds has been investigated up to 30 and 40 GPa, respectively. Utilizing helium as PTM led to the revelation of previously undiscovered isomorphic phase transitions in both $Bi_{14}MoO_{24}$ and $Bi_{14}CrO_{24}$. In $Bi_{14}MoO_{24}$, two distinctive monoclinic phases emerged, supporting our previous findings.[20] On the other side, $Bi_{14}CrO_{24}$ exhibited two novel tetragonal phases before transitioning into a monoclinic phase. Interestingly, the tetragonal phase in both compounds appeared less influenced by the choice of the PTM, as evidenced by a bulk modulus ranging between 48 and 70 GPa, which is dominated by the bismuth−oxygen coordination polyhedra units. Additionally, experiments conducted without no PTM showed an earlier onset of pressure-induced phase transitions compared to those observed with PTM. Moreover, a new cubic phase was identified as coexisting with the high-pressure phases in $Bi_{14}CrO_{24}$. The bulk modulus of this phase was estimated to be 40 GPa, indicating lower values than that of α-Bi_2O_3. These findings underscore the significance of PTM selection in elucidating the intricate phase transitions of complex bismuth materials under high pressure.

■ ASSOCIATED CONTENT

Supporting Information

The Supporting Information is available free of charge at https://pubs.acs.org/doi/10.1021/acs.cgd.4c00904.

Detailed atomic information on the raw materials (Tables S1 and S2), Rietveld refinement of the raw materials (Figures S1 and S2), the goodness of the refinements (Table S3), lattice parameters for different pressures (Tables S4 and S5), proof of the onset phase transition (Figure S3), Le Bail refinement for the high-pressure phases (Figures S4 and S5), proof of the recovered high-pressure phase (Figure S6), equation of state parameters (Tables S6 and S7), proof of the existence of a cubic phase (Figure S7) (PDF)

■ AUTHOR INFORMATION

Corresponding Author

Pablo Botella − *Departamento de Física Aplicada-ICMUV, MALTA Consolider Team, Universitat de Valencia, Valencia 46100, Spain;* orcid.org/0000-0001-6930-8415; Email: pablo.botella-vives@uv.es

https://doi.org/10.1021/acs.cgd.4c00904
Cryst. Growth Des. 2024, 24, 9482−9491

Authors

Josu Sánchez-Martín − *Departamento de Física Aplicada-ICMUV, MALTA Consolider Team, Universitat de Valencia, Valencia 46100, Spain;* orcid.org/0000-0003-0241-0217

Oscar Gomis − *Centro de Tecnologías Físicas: Acústica, Materiales y Astrofísica, MALTA Consolider Team, Universitat Politècnica de València, Valencia 46022, Spain;* orcid.org/0000-0001-6763-0638

Robert Oliva − *Geociències Barcelona (GEO3BCN), CSIC, Barcelona 08028, Spain*

Samuel Gallego Parra − *European Synchrotron Radiation Facility, Grenoble 38043, France;* orcid.org/0000-0001-6516-4303

Julio Pellicer-Porres − *Departamento de Física Aplicada-ICMUV, MALTA Consolider Team, Universitat de Valencia, Valencia 46100, Spain;* orcid.org/0000-0002-4288-900X

Gastón Garbarino − *European Synchrotron Radiation Facility, Grenoble 38043, France*

Frederico G. Alabarse − *Elettra Sincrotrone Trieste, Trieste 34149, Italy;* orcid.org/0000-0002-7375-3666

Srungarpu Nagabhusan Achary − *Chemistry Division, Bhabha Atomic Research Centre, Mumbai 400085, India;* orcid.org/0000-0002-2103-1063

Daniel Errandonea − *Departamento de Física Aplicada-ICMUV, MALTA Consolider Team, Universitat de Valencia, Valencia 46100, Spain;* orcid.org/0000-0003-0189-4221

Complete contact information is available at: https://pubs.acs.org/10.1021/acs.cgd.4c00904

Author Contributions

P.B.: Formal analysis, methodology, writing—original draft, writing—review and editing. J.S.-M.: Data acquisition, writing—review and editing. O.G.: Data acquisition, writing—review and editing. J.P.-P.: Sample preparation (gas loading system), writing—review and editing. G.G.: Sample preparation (gas loading system), data acquisition, writing—review and editing. F.G.A.: Data acquisition, writing—review and editing. D.E.: Conceptualization, formal analysis, writing—original draft, writing—review and editing.

Notes

The authors declare no competing financial interest.

■ ACKNOWLEDGMENTS

The authors gratefully acknowledge the financial support from the Spanish Ministerio de Ciencia e Innovación (DOI: 10.13039/501100011033) under projects PID2022-138076NB-C41 and RED2022-134388-T. D.E. and O.G. thank the financial support of Generalitat Valenciana through grants PROMETEO CIPROM/2021/075-GREENMAT, MFA/2022/007, and MFA/2022/025. D.E. and P.B. thank the financial support of Generalitat Valenciana through grant CIAPOS/2023/406. This study forms part of the Advanced Materials program and is supported by MCIN with funding from the European Union Next Generation EU (PRTR-C17.I1) and by the Generalitat Valenciana. The authors thank Elettra Sincrotrone Trieste (proposal no. 20225011). Additionally, the authors also acknowledge ID15B beamline from the ESRF for providing in-house beamtime.

■ REFERENCES

(1) Frondel, C. Mineralogy of the oxides and carbonates of bismuth. *Am. Mineral.* **1943**, *28*, 521.

(2) Medvedeva, N. I.; Zhukov, V. P.; Gubanov, V. A.; Novikov, D. L.; Klein, B. M. Electronic structure and chemical bonding in δ-Bi_2O_3. *J. Phys. Chem. Solids* **1996**, *57*, 1243−1250.

(3) Jiang, N.; Wachsman, E. D.; Jung, S. H. A higher conductivity Bi_2O_3-based electrolyte. *Solid State Ionics* **2002**, *150*, 347.

(4) Gomez, C. L.; Depablos-Rivera, O.; Medina, J. C.; Silva-Bermudez, P.; Muhl, S.; Zeinert, A.; Rodil, S. E. Stabilization of the delta-phase in Bi_2O_3 thin films. *Solid State Ionics* **2014**, *255*, 147−152.

(5) Zhou, W. Defect fluorite superstructures in the Bi_2O_3-WO_3 system. *J. Solid State Chem.* **1994**, *108*, 381−394.

(6) Ling, C. D.; Withers, R. L.; Schmid, S.; Thompson, J. G. A review of bismuth-rich binary oxides in the systems Bi_2O_3−Nb_2O_5, Bi_2O_3−Ta_2O_5, Bi_2O_3−MoO_3, and Bi_2O_3−WO_3. *J. Solid State Chem.* **1998**, *137*, 42−61.

(7) Zhou, W. Defect Fluorite Superstructures in the Bi_2O_3-WO_3 System. *J. Solid State Chem.* **1994**, *108*, 381−394.

(8) Francesconi, M. G.; Kirbyshire, A. L.; Greaves, C.; Richard, O.; Van Tendeloo, G. Synthesis and structure of $Bi_{14}O_{20}(SO_4)$, A new bismuth oxide sulfate. *Chem. Mater.* **1998**, *10*, 626−632.

(9) Ling, C. D.; Withers, R. L.; Thompson, J. G.; Schmid, S. Structures of $Bi_{14}WO_{24}$ and $Bi_{14}MoO_{24}$ from neutron powder diffraction data. *Acta Crystallogr.* **1999**, *55*, 306−312.

(10) Bu, K.; Luo, H.; Guo, S.; Li, M.; Wang, D.; Dong, H.; Ding, Y.; Yang, W.; Lu, X. Pressure-regulated dynamic stereochemical role of lone-pair electrons in layered Bi_2O_2S. *J. Phys. Chem. Lett.* **2020**, *11*, 9702−9707.

(11) Yedukondalu, N.; Pandey, T.; RakeshRoshan, S. C. Effect of Hydrostatic Pressure on Lone Pair Activity and Phonon Transport in Bi_2O_2S. *ACS Appl. Energy Mater.* **2023**, *6*, 2401−2411.

(12) Levitas, V. I.; Kamrani, M.; Feng, B. Tensorial stress−strain fields and large elastoplasticity as well as friction in diamond anvil cell up to 400 GPa. *npj Comput. Mater.* **2019**, *5*, 94.

(13) Levitas, V. I. Recent In Situ Experimental and Theoretical Advances in Severe Plastic Deformations, Strain-Induced Phase Transformations, and Microstructure Evolution under High Pressure. *Mater. Trans.* **2023**, *64*, 1866−1878.

(14) Wong, S.; Shiell, T. B.; Cook, B. A.; Bradby, J. E.; McKenzie, D. R.; McCulloch, D. G. The shear-driven transformation mechanism from glassy carbon to hexagonal diamond. *Carbon* **2019**, *142*, 475−481.

(15) Gao, Y.; Ma, Y.; An, Q.; Levitas, V.; Zhang, Y.; Feng, B.; Chaudhuri, J.; Goddard, W. A., III Shear driven formation of nano-diamonds at sub-gigapascals and 300 K. *Carbon* **2019**, *146*, 364−368.

(16) Guńka, P. A.; Hapka, M.; Hanfland, M.; Dranka, M.; Chałasiński, G.; Zachara, J. How and Why Does Helium Permeate Nonporous Arsenolite Under High Pressure? *ChemPhysChem* **2018**, *19*, 857.

(17) Argunova, T. S.; Sorokin, L. M.; Pevzner, B. Z.; Balitskii, V. S.; Gannibal, M. A.; Je, J. H.; Hwu, Y.; Tsai, W.-L. The influence of defects in the crystal structure on helium diffusion in quartz. *Phys. Solid State* **2003**, *45*, 1910−1917.

(18) Garg, A. B.; Errandonea, D.; Rodríguez-Hernández, P.; Muñoz, A. ScVO4 under non-hydrostatic compression: a new metastable polymorph. *J. Phys.: Condens. Matter* **2016**, *29*, 055401.

(19) Errandonea, D.; Santamaria-Perez, D.; Achary, S. N.; Tyagi, A. K. Experimental evidence for pressure-driven isostructural and symmetry-breaking phase transitions on $Bi_{14}CrO_{24}$. *Solid State Commun.* **2014**, *182*, 50−54.

(20) Botella, P.; Santamaria-Perez, D.; Otero-de-la-Roza, A.; Oliva, R.; Achary, S. N.; Popescu, C.; Errandonea, D. High-pressure structural phase transition on $Bi_{14}MoO_{24}$. *J. Phys. Chem. Solids* **2023**, *182*, 111598.

(21) Shen, G.; Wang, Y.; Dewaele, A.; Wu, C.; Fratanduono, D. E.; Eggert, J.; Klotz, S.; Dziubek, K. F.; Loubeyre, P.; Fat'yanovAsimowMashimo, O. V. P. D. T.; Wentzcovitch, R. M. M.; Mashimo, T.; Wentzcovitch, R. M. M.; Other members of the

IPPS task group. Toward an international practical pressure scale: A proposal for an IPPS ruby gauge (IPPS-Ruby2020); High Press Res., 2020; Vol. *40*, pp 299−314..
(22) Dewaele, A.; Torrent, M.; Loubeyre, P.; Mezouar, M. Compression curves of transition metals in the Mbar range: Experiments and projector augmented-wave calculations. *Phys. Rev. B* **2008**, *78*, 104102.
(23) Lotti, P.; Milani, S.; Merlini, M.; Joseph, B.; Alabarse, F.; Lausi, A. Single-crystal diffraction at the high-pressure Indo-Italian beamline Xpress at Elettra, Trieste. *J. Synchrotron Radiat.* **2020**, *27*, 222−229.
(24) Poreba, T.; Comboni, D.; Mezouar, M.; Garbarino, G.; Hanfland, M. Tracking structural phase transitions via single crystal x-ray diffraction at extreme conditions: advantages of extremely brilliant source. *J. Phys.: Condens. Matter* **2023**, *35*, 054001.
(25) Prescher, C.; Prakapenka, V. B. DIOPTAS: a program for reduction of two-dimensional X-ray diffraction data and data exploration. *High Pressure Res.* **2015**, *35*, 223−230.
(26) Larson, A. C.; Von Dreele, R. B. *GSAS, General Structure Analysis System*; Los Alamos National Laboratory Report LAUR, 2000; Vol. *86*, p 748.
(27) Momma, K.; Izumi, F. VESTA 3 for three-dimensional visualization of crystal, volumetric and morphology data. *J. Appl. Crystallogr.* **2011**, *44*, 1272−1276.
(28) Toby, B. H. R factors in Rietveld analysis: How good is good enough? *Powder Diffr.* **2006**, *21*, 67−70.
(29) Crumpton, T. E.; Francesconi, M. G.; Greaves, C. The structural chemistry of $Bi_{14}MO_{24}$ (M= Cr, Mo, W) phases: bismuth oxides containing discrete MO_4 tetrahedra. *J. Solid State Chem.* **2003**, *175*, 197−206.
(30) Marciniak, J.; Katrusiak, A. Direct and inverse relations between temperature and pressure effects in crystals: A case study on o-Xylene. *J. Phys. Chem. C* **2017**, *121*, 22303−22309.
(31) Errandonea, D.; Kumar, R. S.; Ma, X.; Tu, C. High-pressure X-ray diffraction study of $SrMoO_4$ and pressure-induced structural changes. *J. Solid State Chem.* **2008**, *181*, 355−364.
(32) Klotz, S.; Chervin, J. C.; Munsch, P.; Le Marchand, G. Hydrostatic limits of 11 pressure transmitting media. *J. Phys. D: Appl. Phys.* **2009**, *42*, 075413.
(33) Aldebert, P.; Traverse, J. P. Etude par diffraction neutronique des structures de haute temperature de La_2O_3 et Nd_2O_3. *Mater. Res. Bull.* **1979**, *14*, 303−323.
(34) Errandonea, D.; Kumar, R. S.; Achary, S. N.; Gomis, O.; Manjón, F. J.; Shukla, R.; Tyagi, A. K. New high-pressure phase and equation of state of $Ce_2Zr_2O_8$. *J. Appl. Phys.* **2012**, *111*, 053519.
(35) Han, Y.; Wang, Q.; Li, S.; Zou, B.; Jiang, J.; Yuan, J.; Zhang, H.; Zhang, G.; Liu, C.; Wang, K. Recent progress in the application of rotational diamond anvil cell. *APL Mater.* **2023**, *11*, 070601.

https://doi.org/10.1021/acs.cgd.4c00904
Cryst. Growth Des. 2024, 24, 9482−9491